VALIDATION OF A METHOD FOR NON-RIGID REGISTRATION OF PROSTATE IMAGES USING FINITE ELEMENT ANALYSIS

Jessica Crouch[1], M.S., Stephen Pizer[1,3], Ph.D., Gikas Mageras[2], Ph.D., Gilad Cohen[2], M.S., Marco Zaider[2], Ph.D., Sarang Joshi[3], Sc.D., and Edward Chaney[3], Ph.D.

[1]Department of Computer Science,
University of North Carolina, Chapel Hill, NC 27599-7512.
[2]Department of Medical Physics,
Memorial Sloan-Kettering Cancer Center, NY, NY 10021
[3]Department of Radiation Oncology,
University of North Carolina, Chapel Hill, NC 27599-7512.

Acknowledgments: This research was supported by research grants P01 CA47982 (UNC) and P01 CA 59017 (MSKCC) from the National Cancer Institute, and a student fellowship grant from Lucent Technologies.

Corresponding Author
Edward L. Chaney, Ph.D.
Radiation Oncology Department CB 7512
University of North Carolina
Chapel Hill, NC 27599-7512
Phone: (919) 966-0300
Fax: (919) 966-7681
Email: chaney@radonc.unc.edu

Running title: Prostate finite element analysis

ABSTRACT

Purpose: Dose escalation to intraprostatic tumor domains detected by magnetic resonance spectroscopy imaging (MRSI) requires non-rigid registration of MRSI-positive volumes (visualized in a prostate gland deformed by the endorectal balloon coil) with ultrasound (US) and/or CT images used for treatment planning. Finite element analysis is a principled method for modeling physical deformation that can be applied for analyzing deformed anatomical structures in medical images. However current implementations of the finite element modeling (FEM) are too laborious and computationally inefficient for routine clinical use. The purpose of this investigation was to validate improved methodology based on deformable m-rep models, for automatically constructing FEM mesh models, defining boundary conditions for the starting and ending states of the deformation process, and efficiently solving the large system of FEM equations to yield a non-rigid transformation. In this paper this approach is referred to as m-rep-based finite element modeling (MFEM).

Methods and Materials: A pelvis phantom was constructed from tissue-like materials to simulate the prostate and surrounding structures including bladder, expandable rectum, and bone. An inflatable balloon simulating the MR coil was placed in the rectal cavity and 75 dummy (non-radioactive) seeds were implanted in the prostate. CT images were acquired with the rectal balloon empty and inflated. The prostate was carefully contoured on all slices and the benchmark coordinates of the centers of all seeds were identified using an interactive point-and-click method. An m-rep model of the relaxed prostate was created by deforming a stock prostate model into the volume defined by the prostate contours. A multiscale FEM mesh model was then automatically generated from the m-rep model. The surfaces of the relaxed and deformed prostate were used to define boundary conditions, and the system of partial differential equations for a linear elastic system was solved using FEM in a computationally efficient multiscalar fashion facilitated by the properties of m-reps. The locations of seeds in the deformed prostate predicted by MFEM were compared to the benchmark coordinates.

Results: The mean error of the MFEM-predicted seed coordinates compared to human labeling in the deformed prostate was slightly less than 1 pixel along the axes in the transverse plane and slightly less than one-half the slice thickness along the cephalo-caudal axis.

Conclusion: The MFEM-predicted seed locations agreed with human labeling within limitations imposed by the experimental conditions such as the discrete nature of the CT data and image artifacts. The automatic meshing algorithm and computational efficiency gained from m-rep methodology offer significant computational improvements that can move finite element modeling closer to clinically practical implementation.

Keywords: Image registration, finite element analysis, m-rep, prostate

INTRODUCTION

The ability to image intraprostatic tumor domains with magnetic resonance spectroscopy imaging (MRSI) offers the potential for targeting localized concentrations of tumor cells for delivery of boost doses of radiation to improve the probability of local control. Implanting radioactive seeds under ultrasound (US) guidance is one approach being investigated for delivering a boost dose (1). The desired accuracy of seed placement for highly localized boost therapy is more demanding compared to a full prostate implant however and thus standard US guided implant procedures do not meet the needs of boost therapy. In particular non-rigid image fusion is required for comparison of US images acquired at the time of implant with MRS images acquired earlier for localizing tumor domains and perhaps CT images for preplanning seed placement. The prostate is essentially relaxed in CT images and deformed to different degrees by endorectal devices in US and MRS images. Rigid registration techniques do not correct for the resulting image differences and thus cannot accurately transfer seed coordinates from one image to another image of the prostate in a different deformed state. When considering possible non-rigid solutions it is important to note that the underlying methodology must be able to accurately predict seed locations for any possible deformed state of the prostate. This requirement can be met by methods that model tissue deformations in a physically correct manner. Finite element analysis is a proven approach that is well established in mechanical engineering and is being applied to the study of human tissues. However, current implementations of FEM involve laborious construction of 3D mesh models and computationally expensive solution of a large system of equations. This paper reports results from a validation study of new methods, based on medial deformable models called m-reps, to automatically generate mesh models from an image, derive boundary conditions from images of deformed objects, and efficiently solve the large system of finite element equations.

METHODS AND MATERIALS

Elastic Properties of Solid Objects

In general a solid object will deform when a stress is applied to its surface. The object's elastic properties describe the physical nature of the deformation process. Objects with isotropic linear elastic properties behave in an ideal manner. The amount of deformation, or strain, is instantaneous and directly proportional to the stress applied, and the deformed object immediately springs back to its original form when the deforming stress is removed. Objects with viscoelastic properties exhibit the more complex behaviors of relaxation, creep, and hysteresis. Relaxation occurs when the stress in an object slowly diminishes as its strain is kept constant. Creep occurs when an object continues to slowly deform as constant stress is applied. Hysteresis occurs when the deformation process is not exactly reversible when the deforming stress is removed.

Extensive knowledge is available about the elastic behavior of many materials such as steel, plastics, and wood. And while the deformation properties of some soft biological materials including lung (2), muscle (3), and brain tissue (4) have been investigated, less information is available about the elastic properties of a number of soft tissue structures including the prostate. At least one study shows evidence that the prostate can be reasonably modeled as a linearly elastic object (5). In addition, other work that involved modeling the prostate also relied on the used a linear elastic prostate model,

with apparent success (6). In the absence of more complete data from experiments with prostate tissue samples that supports a more specialized form of viscoelastic behavior, isotropic linear elasticity is the most reasonable form of elasticity to assume. Even if the prostate is predominately viscoelastic this assumption should be reasonable under conditions where stress and strain are not extreme as in this investigation (7).

Under equilibrium conditions where an object remains stationary, the deformations of an isotropically elastic solid are described by a linear elastic partial differential equation (PDE). The most general form of this equation found in standard text books is given in Equation 1.

$$\mu\nabla^2\vec{u} + (\mu + \lambda)\nabla\left(\nabla^T\vec{u}\right) + \vec{b} = \mathbf{0} \qquad \text{Eqn. (1)}$$

where the vector $\vec{u}$ denotes a function describing the displacement of a point in the object under the influence of a force, $\vec{b}$, on the solid. The constants μ and λ are known as Lamés coefficients and can be determined from Young's modulus and Poisson's ratio. Young's modulus is the ratio of stress to strain for a stress applied along one direction. Poisson's ratio is the amount of an object's contraction perpendicular to an applied stress divided by the amount of elongation parallel to the stress. The relationships between Young's modulus, E, Poisson's ratio, ν and Lamés coefficients are given by Eqns. (2) and (3).

$$E = \frac{\mu(3\lambda + 2\mu)}{\lambda + \mu} \qquad \text{Eqn. (2)}$$

$$\upsilon = \frac{\lambda}{2(\lambda + \mu)} \qquad \text{Eqn. (3)}$$

For the experiments reported here the prostate was assigned E = 60kPa and ν = .495 based on published prostate tissue test results (8). The meshed area exterior to the prostate was assigned E = 10kPa and ν = .3.

Finite Element Modeling

In cases similar to the prostate deformation problem, Eqn. (1) cannot be solved by deriving an analytic solution. Finite element modeling is a method based on fundamental physics principles for modeling mechanical deformations to calculate a solution numerically at a finite number of points, called nodes, in the object (9). Solutions at other points are found by interpolating between nodes. FEM has been applied with good results to medical simulations including maxillo-facial surgery (10), liver surgery (11), and childbirth (12). FEM also has been investigated for non-rigid registration of different images of the same patient (8; 13-15).

The FEM approach assumes that an object undergoing deformation can be modeled as a mesh of solid elements that collectively give a good approximation to the object's

geometric shape and individually undergo compression or extension when subjected to a force (Figure 1). The nodes at which numerical solutions are computed are located at the vertices of the mesh elements. Typical three-dimensions shapes for mesh elements are tetrahedra, pyramids, wedges, and hexahedra, with tetrahedral and hexahedral elements being preferred (Figure 2). Meshes can be comprised of elements of single or mixed shapes. Research has shown that the error in a finite element solution is less for a mesh of linear hexahedral elements than for a mesh of similarly sized linear tetrahedral elements (16).

Solving PDEs such as Equation 1 requires boundary conditions describing specific parameters at the initial and end states of a deformation process. For example the forces causing the mesh to deform can be described, or the vector displacements of points on the object's surface from the initial to the end states of deformation can be specified in detail. In this study m-rep surfaces were used to compute vector displacements.

In the general case creating an FEM mesh for an object is too laborious and time consuming for clinical applications requiring interactive or on-line computer feedback to guide medical decisions or tasks. When dealing with medical images this problem is made more complex by the necessity to first extract the objects of interest from image data. The advantages offered by m-reps are automatic extraction of objects, an object-based coordinate system that facilitates automatic generation of FEM meshes, and means for scaling mesh fineness to solve the FEM system of equations in a computationally efficient coarse-to-fine fashion.

Deformable medial models (m-reps)

M-reps are deformable medial models for representing the interiors and surfaces of 3D objects and groups of objects (17). Objects can have one or more figures, e.g., indentations or protrusions. An m-rep is made from a lattice of medial atoms whose centers are located on the medial sheet - the sheet that defines the middle of an object (Figure 3). Atoms have two radial vectors of equal length extending to points on the surface whose location is implied by the model to within a tolerance proportional to the width of the object. Atoms associated with a crest have a third vector that bisects the two main vectors and touches the peak of the crest.

M-reps are well suited for building models of normal anatomic objects for use in automatic image segmentation, i.e., extracting normal anatomical objects from images (17). The process of building a "stock" m-rep for segmentation includes training the model from a broad sample of particular instances of the corresponding object. Training defines the model geometric properties such as the configuration of the mean model and statistical distributions for shape variations relative to the mean across all training cases. Training also produces statistical distributions for gray scale intensity profiles at many locations around the surface of the object. The profiles define an intensity template against which intensity profiles in the target image are compared to yield an image match term that estimates how well a particular deformed state of the m-rep matches the target image data over the region of the implied boundary. When a trained m-rep is initialized in a target image it undergoes a global transformation that roughly registers the whole m-rep with the corresponding object in the image. Global

transformation is followed by figure-by-figure registration and then atom-by-atom deformations in a cyclic fashion with random order over the medial lattice. A final step displaces the surface implied by the deformed model to closely match the target image data. All transformations and deformations are driven by an algorithm that optimizes an objective function which is the sum of the image match term and a geometric term that measures how well the current deformed state matches the mean m-rep.

One powerful property of m-reps is their object based coordinate system enabled by the atomic-level reference frame illustrated in Figure 3. Each model has its own coordinate system for referencing all points inside and on the surface, and points associated with figures and other models. When an object undergoes deformation the world coordinates of every point inside and on the surface of the object change. However the object based coordinates of each point remain the same, preserving spatial and orientation correspondence between deformed versions of the same object. That is, when the m-rep is deformed the object based coordinates do not change; only the mapping between object and world coordinates changes. The mapping transformation is known at all times so that corresponding points can be referenced in world coordinates. An advantage of preserving point correspondence in object space is that an FEM mesh built to fit a particular m-rep model and expressed in the m-rep's object based coordinates will automatically fit any deformed version of the m-rep model. Another advantage for building meshes is that object-based distance coordinates are expressed as a fraction of object width. This property provides a natural way to scale the dimensions of mesh elements relative to the size of an object, and is particularly powerful for defining progressively finer meshes to facilitate a multiscale approach to solving the FEM system of equations. Progressively finer meshes conform better to the shape of the object because the elements are not simply subdivisions of coarser mesh elements but are computed using the same algorithm used for coarse grids that places element nodes directly on the object surface. Better conformance to the object shape contributes to the improved precision offered by finer m-rep generated meshes.

M-rep Based Meshing

This work evaluates the performance of two algorithms discussed in detail by Crouch (18) and reviewed briefly here. One algorithm automatically generates a mesh from an m-rep segmentation of an image and defines boundary conditions for the beginning and end stages of the deformation. The other is an efficient solution algorithm that takes advantage of the multi-scale nature of solving the FEM system of equations.

The meshing algorithm constructs a hexahedral mesh for each object and for the space separating multiple objects. Mesh properties are determined completely by information contained in the m-rep model, eliminating the need for user interaction. Since an m-rep model of a prostate has only a main figure, the single-figure version of the algorithm is discussed here. The first step is to construct a sampling grid on the medial surface of the segmented prostate. The vertices of the sampling grid are placed at regular intervals in the object coordinate frame. The grid spacing is determined by the ratio of the average width of the object to the average distance between medial atoms in world space. This spacing produces hexahedral elements with approximately equal dimensions. The coordinates of other layers of nodes are derived from the sampling grid. For sample points on the interior of the grid, five nodes are created. For sample

points on the edge of the grid, associated with a crest region, a sixth node is created positioned on the object crest. A resulting two-dimensional mesh pattern is illustrated in Figure 1. The prostate meshs for the three mesh levels in this study are shown in Figure 4. Figure 5 shows undeformed and deformed prostate meshes superimposed on CT data.

The meshing process generates a regular hexahedral mesh in object space. When the mesh is mapped to world coordinates, where FEM is performed, the shapes of most transformed elements are well suited for FEM calculations (Figure 6). However some elements can have geometries that are distorted which leads to folds in the mapping transformation. Such distortions can degrade the accuracy of FEM calculations, and thus further analysis is performed to detect and correct flawed elements in world space (18). This mesh optimization process successfully produced meshes for the prostate which meet well established criteria for a high quality solution to the FEM system of equations (16).

Space external to m-rep models

The male pelvis contains multiple objects that must be meshed to solve a general deformation problem. In this study however the only object of interest is the prostate, and thus individual mesh models for other objects does not improve accuracy or provide additional information. For this reason the tissues and structures around the prostate were treated as homogeneous linearly elastic material. This space around the prostate needed to be meshed as well, but a different approach was used since the space was not modeled by m-reps. First a layer of pyramids was automatically built on top of the hexahedral elements generated by the m-rep meshing algorithm. Then the remainder of the volume of interest was filled with tetrahedra using existing software called CUBIT available from Sandia National Laboratories (19). The pyramid and tetrahedral elements filling the space external to m-rep models are shown in Figure 4.

It should be noted that CUBIT was not considered suitable for generating meshes for m-rep models for the two important reasons related to solution quality and computational efficiency. First, CUBIT generates tetrahedral meshes, but reliable hexahedral meshing is not available. As mentioned in the section on Finite Element Modeling, linear hexahedral meshes offer better solution accuracy than linear tetrahedral meshes. Second, the m-rep meshing algorithm provides a reasonably good solution estimate that can be iteratively refined. The solution estimate is not available from CUBIT or other meshing software.

Boundary Conditions

The FEM solution of PDEs requires boundary conditions specified in terms of either applied forces or vector displacements of points on the surface of the object undergoing deformation. Images provide information about the effects of forces but no direct information about the forces themselves. And although the surfaces of the undeformed and deformed object can be identified, only with the aid of a solid model and an object representation such as that provided by m-reps can the vector displacements be automatically derived from surface deformations observed in two images.

Boundary conditions are established in the following manner for the prostate. The m-rep segmentation of the undeformed prostate, including the mesh generated as described above, is transferred onto the image of the deformed prostate and used as a model to segment the deformed prostate. The m-rep models for the undeformed and deformed prostates have the same topology and their object-based coordinates span exactly the same parameter space. This correspondence means that the object based coordinate system defines a one-to-one geometry-based correspondence between points in the relaxed and deformed prostates. The algorithm examines each node of the hexahedral mesh that lies on the prostate surface and computes a vector displacement in world coordinates. To be consistent with physically realistic modeling, the solution to the system of equations is optimized by minimizing the work expended to produce the displacements. For a linearly elastic system, as assumed for this study, the work expended is equal to the change in the elastic potential energy given by Equation (4).

$$PE = \tfrac{1}{2}\int_V \vec{\sigma} \bullet \vec{\varepsilon} dV - \int_V \vec{b} \bullet \vec{u} dV - \int_S \vec{t} \bullet \vec{u} dS \qquad \text{Eqn. (4)}$$

where

- PE = elastic potential energy
- $\vec{\sigma}$ = stress
- $\vec{\varepsilon}$ = strain
- $\vec{b}$ = body force applied to object
- $\vec{u}$ = vector function describing node displacement
- $\vec{t}$ = surface force applied to object

In this investigation body forces such as gravity were ignored and surface forces were not modeled. Thus the first term on the left side of Equation (4) is minimized to optimize the boundary conditions.

Efficient Solution Algorithm

To deform a mesh using FEM, an NxN system of linear equations must be solved, where N is the number of nodes in the mesh. Approaches that use fine meshes, i.e., large N, are computationally expensive. Fortunately the large systems of equations encountered in a coarse-to-fine-mesh approach can be more efficiently solved by borrowing an idea from multigrid theory (20, 21). In multigrid theory an iterative solver is applied at each grid level, i.e., mesh size in this study, to improve the approximation at that level, and then the approximation is transferred to a different grid and the process is repeated. A scheduling algorithm determines the order in which grid levels are visited. The approach taken in this study was to estimate the solution using m-rep geometry correspondences, apply a conjugate gradient algorithm to refine it iteratively, and then interpolate the solution to a finer mesh. The conjugate gradient algorithm was applied to the finer mesh to further improve the solution. An arbitrary number of interpolation and refinement steps is possible, but only three mesh levels were used in this study. The number of iterations required to converge to a solution was reduced due to the good approximation from the initial coarse mesh. The numbers of nodes and elements for each mesh level are shown in Table 1.

EXPERIMENTAL PROCEDURE

For the purpose of validating the algorithm, a pelvis phantom was constructed from tissue-like materials to simulate the prostate and surrounding structures including bladder, expandable rectum, seminal vesicles, and bone (CIRS, Norfolk, VA). All simulated organs were made of zerdine® (a water based polymer) as was the background phantom material. Pelvic bone was simulated with epoxy. An inflatable balloon simulating the MR rectal coil was placed in the rectal cavity and 75 dummy radioactive seeds were implanted in the prostate. According to the manufacturer, zerdine was made to simulate the ultrasound characteristics of human liver tissue. The speed of sound, acoustic attenuation, and backscatter properties of this material can be adjusted to simulate different tissues. Thus, the contrast for different structures (built by molding zerdine in the respective shapes) is such that they are visible using both ultrasound and CT (the prostate is darker than background material, urethra material is darker than prostate, etc.). To track the deformation of the prostate, seventy-five “dummy” seeds were placed within the simulated gland in a quasi-regular pattern (Figure 7). To simulate the deformation of the prostate by the MRS probe, the rectum was simulated by an empty space into which the MRS probe was inserted. Inflation and deflation of the probe inside the phantom thus produced the same type of deformation produced by an endo-rectal probe.

CT images with 3 mm slice thickness and .78 mm x.78 mm pixel size in the transverse plane were acquired with the rectal balloon empty and inflated. The prostate was carefully contoured and the benchmark centers of the seeds were defined in the CT data using and interactive point-and-click method. The CT data was windowed and the window was centered so that only very bright pixels were displayed, facilitating identification of pixels near the seed centers.

At the time of this study a fully trained m-rep model for segmenting the prostate from a gray-scale CT image was not available. To obtain m-rep segmentations, the gray-scale CT images were replaced with a binary images created from the prostate contours. The

prostate was segmented in the binary images with an m-rep prostate model and an analytic Gaussian-based image match term that gave a strong response at the prostate boundary. An FEM mesh model was then automatically generated from the m-rep model of the undeformed prostate as described in the section on M-rep Based Meshing.

The m-rep surfaces of the undeformed and deformed prostate were used to define boundary conditions in terms of vector displacements. The FEM system of equations for the deformation process was solved in a multiscalar fashion as described in the section discussing the Efficient Solution Algorithm. The CALFEM package (22) was selected as the core software for assembling and solving the equations. CALFEM is a finite element package from the Department of Mechanics and Materials at Lund University that is written in MATLAB (23). The CALFEM code was modified to handle tetrahedral and pyramid elements as well as hexahedral elements, but the logic was not changed. The solution step was accomplished with a conjugate gradient solver that is a standard module of MATLAB.

The output of interest from the above computations was the transformation function for mapping the undeformed FEM mesh onto the deformed prostate. This transformation was applied to the seed locations in the undeformed prostate to predict the seed locations in the deformed prostate.

RESULTS AND DISCUSSION

The MFEM-predicted locations of the 75 seeds implanted in the phantom prostate were compared to benchmark coordinates. The comparison between the predicted and benchmark seed locations is presented in Table 2 for the three mesh subdivision levels and for unoptimized and optimized boundary conditions. Figures 7 and 8 show agreement of MFEM-predicted seed locations with image data for a selected transverse plane.

Table 3 shows the incremental improvement in all error categories gained from computing the deformation over successively finer meshes. It is conceivable that further improvements could be realized by going to even finer meshes. However the mean errors for the finest mesh (level 3) are smaller than the dimensions of a single voxel, which is an excellent result under the conditions of this experiment.

The overall best agreement is obtained for the finest mesh level (level 3) where the total mean error over all 75 seeds is .2 cm. The mean errors along the x and y axes in the transverse plane are .0766 cm and .0761 cm respectively, less than one pixel width along both axes. As would be expected for the direction of poorest spatial resolution, the largest component of the total error is along the cephalo-caudal axis (z axis) where the mean error is .1393 cm, less than half the slice thickness.

Figure 9 shows the histograms for errors along the x, y, and z axes. The maximum disagreement in the transverse plane was less than 4 pixels in the x direction and less than 3 pixels in the y direction. The maximum disagreement in the x direction occurred for a single outlier; otherwise the histograms are comparable for the x and y directions. The standard deviation for both axes in the transverse plane was about three-fourths of a pixel. Along the z axis the maximum disagreement was about 1.5 times the slice

thickness for three seeds. For the remainder of the seeds the maximum disagreement along the z axis was within the thickness of a single slice. The standard deviation along the z axis was about one-third of the slice thickness.

The difference between unoptimized and optimized boundary conditions is that the work required for deformation (Equation 4) was minimized for the optimized boundary conditions. The results in Table 2 show that optimization did not improve agreement in this investigation. This result may follow from the fact that the deformation created by the inflated balloon in this study, while representative of actual clinical situations, was fairly mild. Under these circumstances Equation 4 may be moderately insensitive to differences in paths taken by nodes in the prostate to traverse the moderate distance from their relaxed to deformed positions. However further study is needed to understand the effects and importance of optimizing boundary conditions for deformed tissues.

For the results reported in Table 2 the prostate was assigned a Young's modulus of 60kPa and □□□□□□□□□□□□□ of .495 (8). FEM methods in general are sensitive to the particular values of Young's modulus and Poisson's ratio. However compared to methods like MFEM that specify boundary conditions in terms of the undeformed and deformed surfaces, FEM methods that describe boundary conditions in terms of applied forces are more sensitive to Young's modulus. This result is expected since Young's modulus is defined in terms of the applied forces. As seen from the results shown in Table 4, the MFEM methodology is insensitive changes in Young's modulus over a couple orders of magnitude, but is sensitive to Poisson's ratio.

Error Evaluation

The primary sources of error contributing to the observed differences between MFEM predictions and benchmark coordinates can be separated into two categories: 1) experimental conditions, and 2) MFEM algorithm errors in computing the deformation. Experimental conditions affecting the observed error include 1) the discrete nature of the CT image data; 2) partial volume and streaking artifacts; and 3) human errors in contouring the prostate. The MFEM method is quite complex and involves many calculations that can contribute to the observed error. The most significant potential sources of error are 1) differences between prostate tissue mechanics and the linear elastic model; 2) specific elastic properties assigned to the prostate; and 3) discretization of the solution space.

In this experiment the exact coordinates of seeds were unknown and were estimated using an interactive point-and-click method. Thus the errors reported in this study are related to the comparison of human-identified benchmarks (Figure 10). The properties of the CT image data affects the quality of the benchmark coordinates. The discrete nature of the image data essentially means that the limiting accuracy of an interactive method for finding seeds under ideal imaging conditions is determined by voxel dimensions. The best a human can do using a point-and-click method is to localize the center of a seed to a particular voxel. If this task were performed correctly in every instance, the precision (reproducibility) would be half a pixel (.39 mm) in the transverse plane and half the slice thickness (1.5 mm) along the z axis, for a total reproducibility of 1.6 mm computed as the square root of the sum of the squares for all three axes. In real images these limiting values are degraded by artifacts. For example since seeds were

4.5 mm long, each seed appeared in at least two slices and sometimes three. In the transverse plane streaking artifacts obscured the cross sections of seeds. Unfortunately the effects of imaging artifacts on seed identification cannot be assessed for the images used in this study. However the observed standard deviation of 2.0 mm compares quite well to the ideal limiting precision of 1.6 mm.

Errors in the contours defining the boundary conditions for computing the deformation can introduce inaccuracies in the computed seed positions. To examine the effect of segmentation error, five perturbed versions of the prostate m-rep model from the image of the deformed prostate were created. The mesh mapping transformation was computed for each of the perturbed models, and the seed displacement error estimates were calculated for each of those mappings. The original m-rep model from the inflated probe image has a volume of 39.22 cm^3, and is pictured in Figure 11 along with the perturbed models. A description of each of the perturbed models follows, and the error estimates for each model are presented in Table 5.

1. Perturbed model with a flat end and a volume of 36.06 cm^3.
2. Perturbed model with a depression .6 cm deep on the top surface and a volume of 38.46 cm^3.
3. Perturbed model with a bump .6 cm high on the top surface and a volume of 40.06 cm^3.
4. Perturbed model with a depression .6 cm deep on the bottom surface and a volume of 38.38 cm^3.
5. Perturbed model with a bump .6 cm high on the bottom surface and a volume of 40.23 cm^3.

These results in Table 5 show that segmentation errors do lead to an increase in registration error, as expected. The amount of registration error is related to the extent of the segmentation error and the location of the segmentation error. For the prostate model, a segmentation error on the prostate's lower surface had a more detrimental effect than a similar error on the prostate's upper surface. In this study the edge of the prostate was clearly visible on most but not all slices, leading to a high level of confidence that contouring errors were small. Based on this confidence and the results in Table 5, the effects of contouring errors are thought to be small compared to other sources of error.

The material for constructing the prostate phantom is not known to be an ideal, homogeneous linearly elastic solid, especially in the presence of implanted seeds. To the extent that the mechanical behavior of the material deviates from the linear elastic model, the model will provide inaccurate predictions. Within the limits of the relatively mild deformation in this study the deviation from an ideal is assumed to be small compared to other effects.

The solution to the linear elastic equations is approximated at a finite number of nodes on the MFEM mesh. The error in the solution due to this discrete approximation can be made arbitrarily small by using a very fine mesh as illustrated in Table 2. At mesh level

3 and higher, other components of the error outweigh the discretization component.

CONCLUSION

The MFEM-predicted seed locations agreed with human labeling within limitations imposed by the experimental conditions such as the discrete nature of the CT data and image artifacts. The automatic meshing algorithm and computational efficiency gained from m-rep methodology offer significant computational improvements that can move finite element analysis closer to clinically practical implementation.

LITERATURE CITED

1. Zaider M, Zelefsky MJ, Lee EK, Zakian KL, et al. Treatment planning for prostate implants using magnetic-resonance spectroscopy imaging. Int J Radiat Oncol Biol Phys 2000;47:1085-96.

2. Maksym GN and Bates JHT. A distributed nonlinear model of lung tissue elasticity. J Applied Phys1997; 82:32–41.

3. Pidaparti RM, Liu Y, and Meiss RA. A viscoelastic material model to represent smooth muscle shortening. J Bio-Medical Materials and Engr1997;7:171–177.

4. Miller K and Chinzei K. Modelling of Brain Tissue Mechanical Properties; Bi-Phasic Versus Single-Phase Approach," in J. Middleton, M. L. Jones, and G.N. Pande (eds.) Computer Methods in Biomechanics & Biomedical Engineering - 2, Gordon and Breach Science Publishers, The Netherlands1998; 535-542.

5. Krouskop TA, Wheeler TM, Kallel F, et al. Elastic moduli of breast and prostate tissues under compression. Ultrasonic Imaging1998; 20: 260–274.

6. Bharatha A, Hirose M, Hata N, et al. Evaluation of three-dimensional finite element-based deformable registration of pre-and intraoperative prostate imaging. Med Phys 2001; 28:2551–2560.

7. Fung YC. Biomechanics: Mechanical Properties of Living Tissues. Springer, New York, Second edition, 1993.

8. Krouskop TA, Wheeler TM, Kallel F, et al. Elastic moduli of breast and prostate tissues under compression. Ultrasonic Imaging1998, 20:260–274.

9. Bathe K. Finite Element Procedures. Upper Saddle River, New Jersey. Prentice-Hall, 1996.

10. Chabanas M and Payan Y. A 3D finite element model of the face for simulation in plastic and maxillo-facial surgery. Proceedings, Third International Conference on Medical Image Computing and Computer- Assisted Intervention (MICCAI) 2000, pp 1068-1075.

11. Cotin S, Delingette H, and Ayache N. Real-time elastic deformations of soft tissues for surgery simulation. IEEE Transactions On Visualization and Computer Graphics1999, vol. 5(1), pp. 62–73.

12. Lapeer RJ and Prager RW. Finite element model of a fetal skull subjected to labour forces. Proceedings, Second International Conference on Medical Image Computing and Computer-Assisted Intervention (MICCAI) 1999, pp 1143-1155.

13. Mohamed A, Davatzikos C, and Taylor R. A combined statistical and biomechanical model for estimation of intra-operative prostate deformation. Proceedings, Fifth

International Conference on Medical Image Computing and Computer-Assisted Intervention (MICCAI) 2002, pp 452–460.

14. Ferrant M, Warfield SK, Nabavi A, et al. Registration of 3D MR images of the brain using a finite element biomechanical model. Proceedings, Third International Conference on Medical Image Computing and Computer-Assisted Intervention (MICCAI), 2000, pp 176-185.

15. Azar FS, Metaxas DN, and Schnall MD. Methods for modeling and predicting mechanical deformations of the breast under external perturbations. Medical Image Analysis 2002; 6 (1): 1-27.

16. Benzley SE, Perry E, Merkley K, et al. A comparison of all hexagonal and all tetrahedral finite element meshes for elastic and elasto-plastic analysis. Proceedings, 4th International Meshing Roundtable1995: 179–191.

17. Pizer SM, Chen JZ, Fletcher PT, et al. Deformable m-reps for 3D medical image segmentation. International Journal of Computer Vision 2003 (submitted). Available on-line at
http://midag.cs.unc.edu/pubs/papers/IJCV01-Pizer-mreps.pdf.

18. Crouch J, Pizer SM, Chaney EL, and Zaider M. Medial Techniques to Automate Finite Element Analysis of Prostate Deformation. Transactions on Medical Imaging 2003 (submitted). Available on-line at http://midag.cs.unc.edu/pubs/papers/TMI03-Crouch-FEM.pdf

19. CUBIT: http://endo.sandia.gov/cubit/.

20. Trottenberg U, Oosterlee C, and Schüller A. Multigrid. Academic Press, 2001.

21. Wesseling P. An Introduction to Multigrid Methods. John Wiley and Sons, 1992.

22. CALFEM, a finite element toolbox to MATLAB. Department of Mechanics and Materials, Lund University, Lund, Sweden, 1999. http://www.byggmek.lth.se/Calfem/.

23. MATLAB, http://www.mathworks.com/.

FIGURES

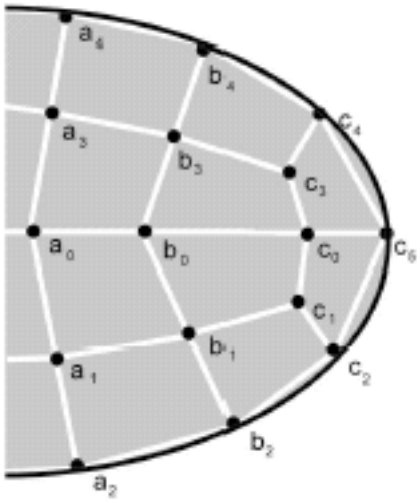

Figure 1. Example of a two-dimensional finite element mesh automatically generated from an m-rep model. Notice that the mesh closely models the shape of the object. The nodes in the mesh are labeled a_i, b_i, and c_i. The nodes a_0, and b_0 are samples on the center portion of the medial surface and give rise to nodes a_0 - a_4 and b_0 - b_4, respectively. The node c_0 is a sample on the perimeter of the medial surface and give rise to nodes c_0 - c_5.

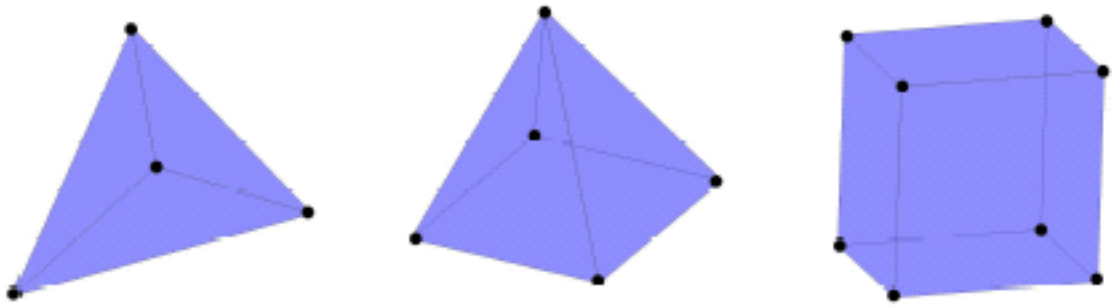

Figure 2. Three-dimensional mesh elements. **Left:** Tetrahedral element. **Center:** Pyramid element. **Right:** Hexahedral element.

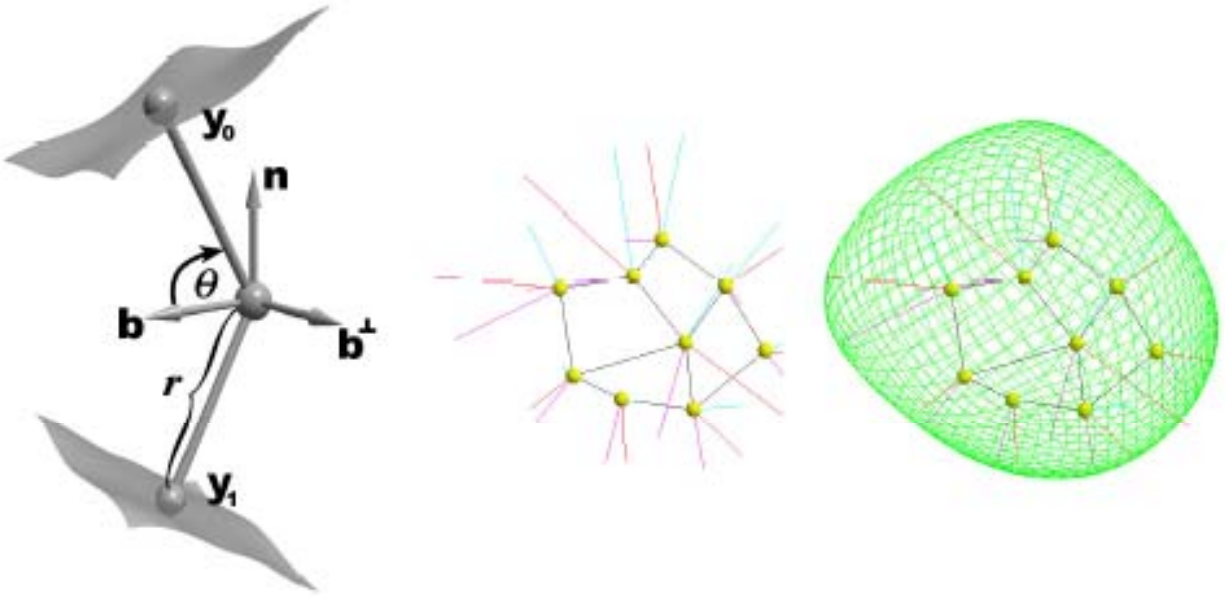

Figure 3. Left: Diagram of a medial atom. The atom hub is shown as a ball at the center. Radiating from the hub are two spokes ***y*** and $\boldsymbol{y_0}$ of length r. The object's surface implied by the atom is perpendicular the spokes at their tips. Attached to the hub is a reference frame ($\mathbf{n},\mathbf{b},\mathbf{b}^{\perp}$). **b** is the unit vector bisecting the angle 2ϑ between the radial spokes; $\mathbf{b}^{\perp}$ is the unit vector perpendicular to the plane defined by **b**, ***y*** and $\boldsymbol{y_0}$; and **n** is the unit vector perpendicular to **b** and $\mathbf{b}^{\perp}$. The reference frame provides the basis for the object-based coordinate system associated with m-rep models. **Center:** A single figure m-rep model of the prostate composed of a lattice of medial atoms. **Right:** Prostate m-rep with wireframe implied surface. Notice that atoms on the periphery of the medial lattice have a third radial spoke extending to the tip of the crest.

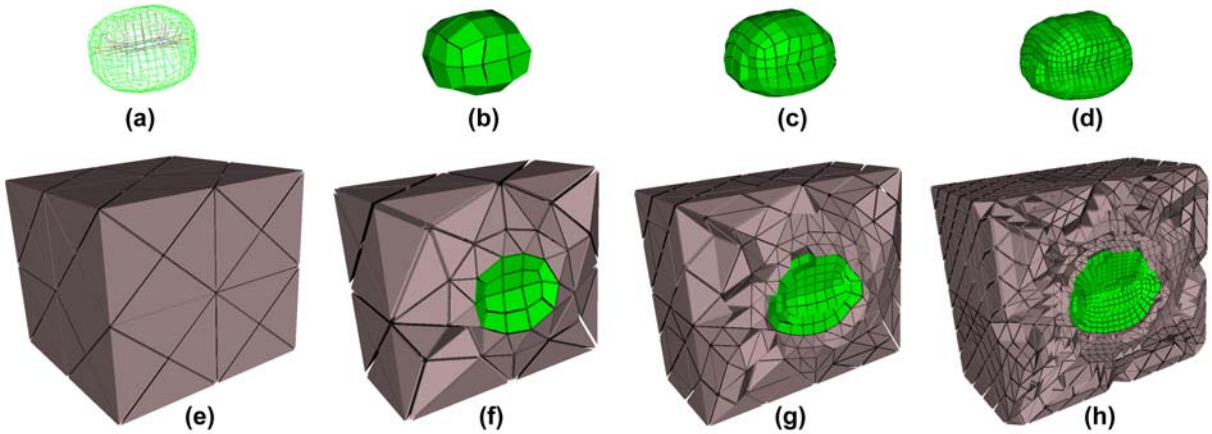

Figure 4. Prostate meshes at three scale levels. (a) Prostate m-rep model. (b) Level 1 prostate mesh (coarse). (c) Level 2 prostate mesh. (d) Level 3 prostate mesh (fine). (e) Exterior view of entire meshed volume. (f) Sliced view of level 1 meshed volume. g) Sliced view of level 2 meshed volume. (h) Sliced view of level 3 meshed volume.

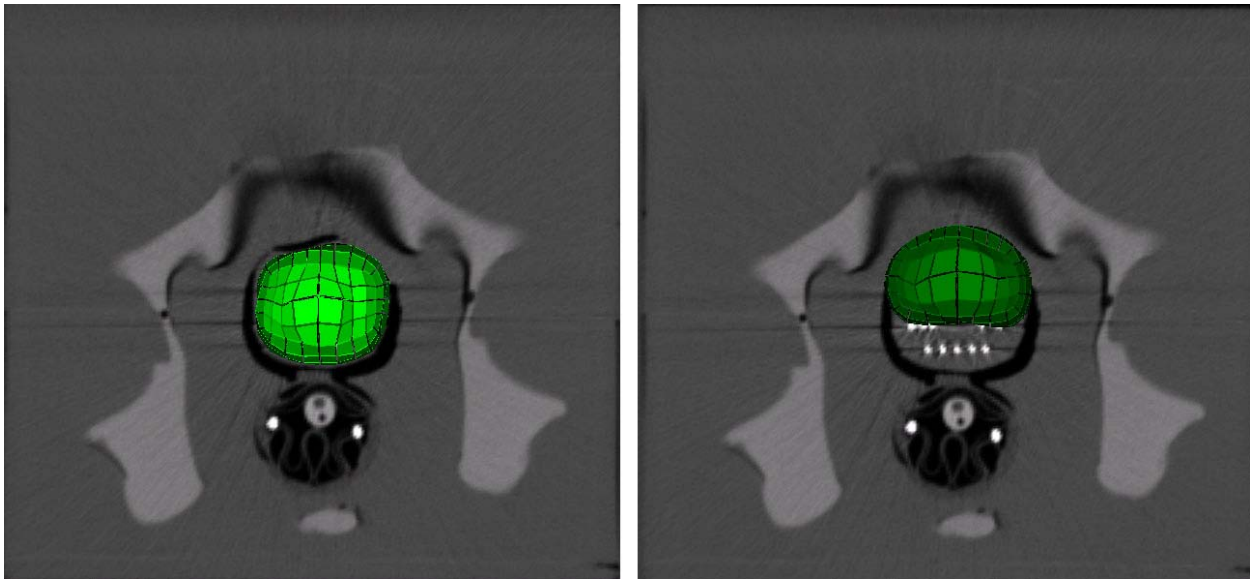

Figure 5. Left: Undeformed level 2 prostate mesh overlaid on a slice of the corresponding image. **Right:** Deformed level 2 prostate mesh overlaid on the same slice.

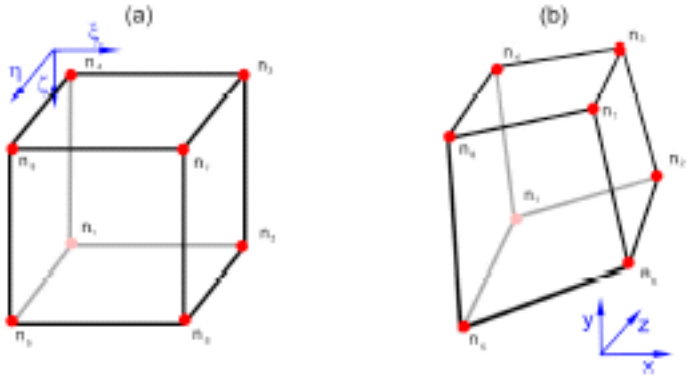

Figure 6. Left: Hexahedral element in object related parameter space. **Right:** Hexahedral element mapped into world space. Corresponding nodes are labeled.

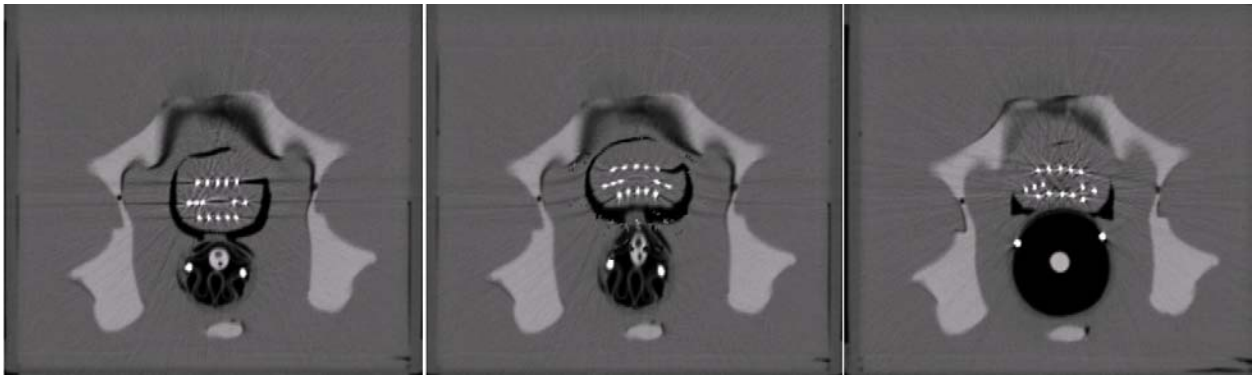

Figure 7. **Left:** CT Slice of the phantom prostate with uninflated probe. **Center:** Same slice as left, after MFEM-computed deformation has been applied. **Right:** CT slice of the phantom prostate with inflated probe.

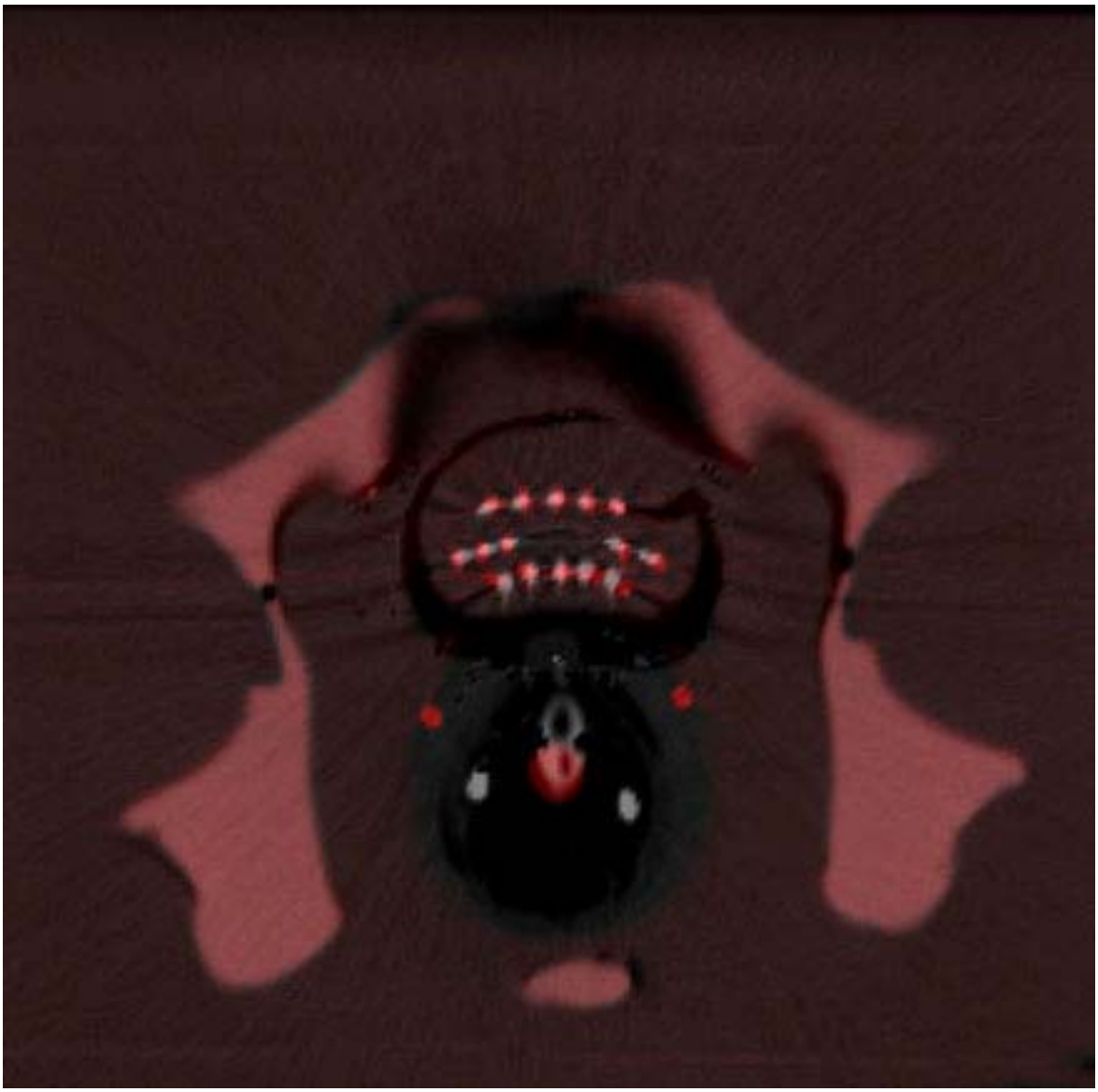

Figure 8. Computed seed positions (red) overlaid on the corresponding CT slice through the deformed prostate. This image illustrates how well the computed positions match the actual imaged positions.

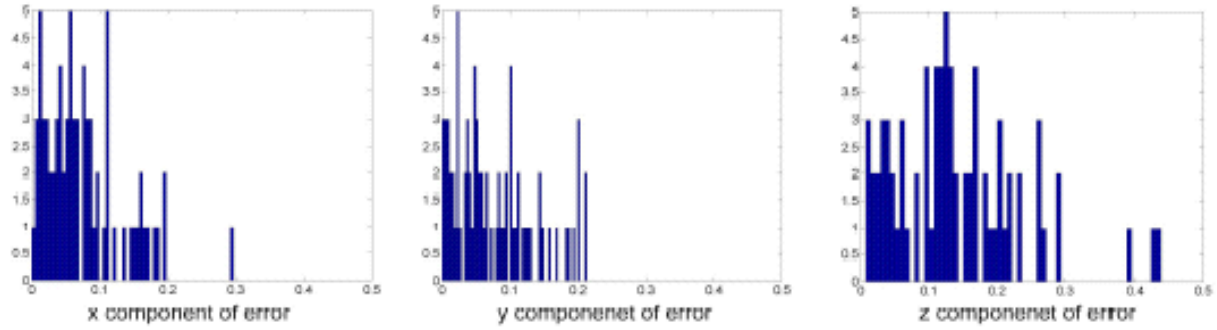

Figure 9. Histograms for errors along the x, y, and z axes of the CT images.

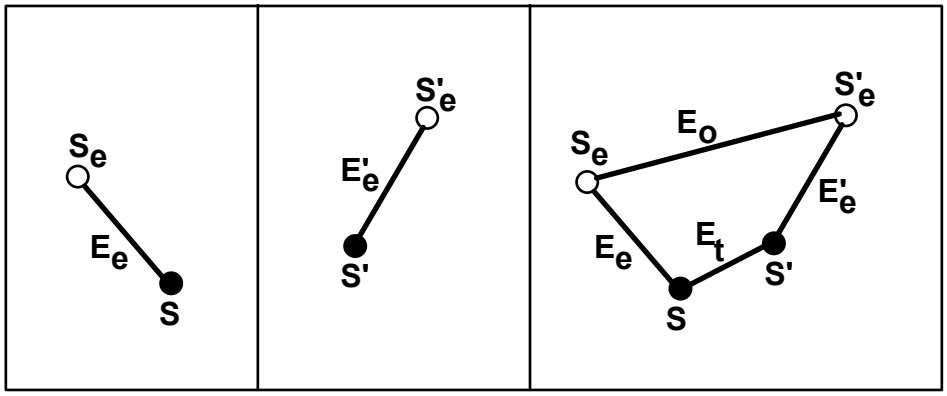

Figure 10. Illustration of error analysis for a single seed. Graphs are shown in two dimensions but generalize to three dimensions. **Left:** The true and human-estimated source positions, S and S_e respectively, in the CT of the undeformed prostate. The true position S is unknown. The random human error associated with estimating S is E_e. **Center:** Unknown true and human-estimated source positions, S' and S'_e respectively, in the CT of the deformed prostate. The random human error is E'_e. **Right:** After finite element computations, the computed deformation is used to map the coordinates of S_e onto the image of the deformed prostate. The error observed in this study is E_o. The true error E_t could not be measured.

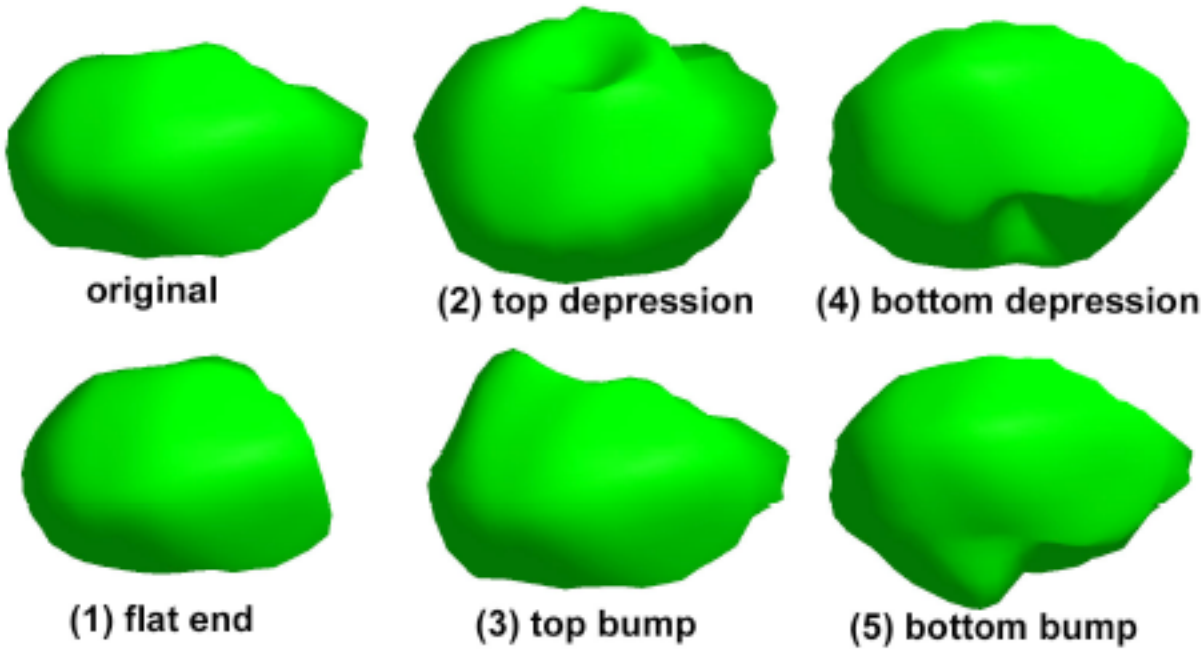

Figure 11. Perturbed prostate models used to examine the effect of segmentation errors on the predicted locations of seeds in the deformed prostate.

TABLES

Table1. Complexity of Subdivided Mesh Levels

Mesh Subdivision Level	Total Node Count	Total Element Count	Hexahedral Element Count	Pyramid Element Count	Tetrahedral Element Count
1	254	836	76	52	708
2	1,836	6,792	608	312	5,872
3	14,068	54,960	4,864	1,872	48,224

Table 2. Error estimates for the predicted seed locations that result from the uninflated-to-Inflated mapping. All errors are in units of centimeters and are averages of the measurements for each of the 75 seeds. The x and y components lie in a high resolution image plane. The z component lies across the image planes. Errors are stated in units of cm.

	Mesh Sub-division Level	Total error	Total std dev	x error	x std dev	y error	y std dev	z error	z std dev
Unoptimized boundary conditions	1	.2273	.0934	.1043	.0642	.0696	.0641	.1608	.1036
	2	.2044	.0790	.0857	.0617	.0666	.0534	.1474	.0893
	3	.1999	.0808	.0763	.0580	.0764	.0599	.1392	.0930
Optimized boundary conditions	1	.2705	.0869	.1308	.0785	.1026	.0776	.1730	.1057
	2	.2054	.0799	.0852	.0605	.0679	.0547	.1485	.0900
	3	.2000	.0807	.0766	.0580	.0761	.0598	.1393	.0928

Table 3. Amount of change in predicted seed locations produced by computing the deformation using finer subdivision levels. Error changes are stated in units of cm.

Mesh level	Total error decrease	Total std dev decrease	x error decrease	x std dev decrease	y error decrease	y std dev decrease	z error decrease	z std dev decrease
1→2	.1006	.0515	.0496	.0349	.0493	.0392	.0542	.0470
2→3	.0374	.0169	.0148	.0111	.0224	.0182	.0174	.0146

Table 4. Effects of Poisson's ratio and Young's modulus on observed error. Error values are stated in units of cm.

Young's Modulus	Poisson's Ratio	Total error	Total std dev	x error	x std dev	y error	y std dev	z error	z std dev
6 kPa	.495	.2044	.0790	.0857	.0617	.0666	.0534	.1473	.0893
60 kPa	.495	.2044	.0790	.0857	.0617	.0666	.0534	.1474	.0893
600 kPa	.495	.2044	.0790	.0857	.0617	.0666	.0534	.1474	.0893
60 kPa	.3	.2207	.0818	.0900	.0621	.0720	.0619	.1592	.0961
60 kPa	.35	.2156	.0802	.0870	.0608	.0694	.0583	.1570	.0945
60 kPa	.40	.2101	.0781	.0834	.0594	.0666	.0551	.1543	.0929
60 kPa	.45	.2048	.0761	.0799	.0583	.0643	.0533	.1511	.0909
60 kPa	.495	.2044	.0790	.0857	.0617	.0666	.0534	.1474	.0893

Table 5. Effects of segmentation errors on observed error. Error values are stated in units of cm.

Perturbed model	% vol. change	Total error	Total std dev	x error	x std dev	y error	y std dev	z error	Z std dev
Original	0%	.2044	.0790	.0857	.0617	.0666	.0534	.1474	.1309
Flat end	-8.1%	.3016	.0995	.1162	.0809	.1568	.0772	.1828	.1309
Top depression	-1.9%	.2062	.0835	.0850	.0623	.0757	.0684	.1408	.0911
Top bump	+2.1%	.2176	.0827	.0979	.0690	.0786	.0601	.1474	.0922
Bottom Depression	-2.14%	.2567	.1719	.1045	.0906	.1417	.1586	.1562	.1117
Bottom bump	+2.6%	.2771	.1237	.1068	.0823	.1443	.1476	.1524	.0912